

Localized Chiral Magnetic Effect in equilibrium QCD

B. B. Brandt, G. Endrődi, E. Garnacho-Velasco, G. Markó, and A.D.M. Valois

*Fakultät für Physik, Universität Bielefeld,
Universitätsstraße 25, 33615 Bielefeld, Germany*

(Dated: September 27, 2024)

We study the impact of a non-uniform magnetic background field on the Chiral Magnetic Effect (CME) in equilibrium QCD using lattice simulations with 2+1 flavors of dynamical staggered quarks at the physical point. We show that in the presence of a non-uniform magnetic field the CME manifests itself via a localized electromagnetic current density along the direction of the field, which integrates to zero over the full volume. Our primary observable is the leading-order coefficient of the current in a chiral chemical potential expansion, which we compute for various lattice spacings and extrapolate to the continuum limit. Our findings demonstrate that, even though the global spatial average of the CME conductivity vanishes in equilibrium, steady currents still exist locally. Thus, spatially modulated magnetic fields provide a possible way of generating a non-trivial CME signal in equilibrium.

I. INTRODUCTION

Heavy-ion collision (HIC) experiments provide an exceptional environment to investigate strongly interacting matter by exposing it to extreme conditions. A prime example of effects arising in this context are anomalous transport phenomena. These effects relate quantum anomalies with electromagnetic fields and vorticities, producing a series of non-dissipative currents which are the subject of extensive theoretical and experimental studies (see Ref. [1] for a recent review). Being intimately related to anomalies, these effects effectively probe the topological nature of the vacuum of Quantum Chromodynamics (QCD).

The most celebrated among anomalous transport phenomena is the Chiral Magnetic Effect (CME): the generation of an electromagnetic current in a magnetized and chirally imbalanced system [2]. This effect is now understood as an out-of-equilibrium phenomenon, which has been linked with negative magnetoresistance in Dirac semimetals [3] and is actively sought for in heavy-ion collision experiments [4–6]. In systems in thermal equilibrium, a global CME current is absent. This can be understood as a direct consequence of the quantum-field-theoretical generalization of Bloch’s theorem, which forbids global conserved currents to flow in equilibrium [7]. On the quantum field theory level, regularization plays a crucial role in the absence of the CME current [8–12]. In lattice regularization for example, the use of a conserved vector current is of particular importance [13].

The vast majority of studies of anomalous transport effects, CME in particular, have focused on homogeneous magnetic fields. However, the magnetic fields created in heavy-ion collisions are far from being uniform [14]. These inhomogeneous fields have already been shown to have a sizeable effect on QCD observables [15]. In this letter, we will use lattice QCD simulations to investigate the impact of such magnetic fields on the chiral magnetic effect. Lattice simulations have been widely used to study anomalous transport effects [9, 11, 13, 16–21], as well as to investigate the role of non-uniform magnetic fields in

QCD [15, 22] (see the review [23]), providing an ideal framework to study the relation between these. The impact of weak inhomogeneities on the CME has also been studied within the Wigner-Weyl formalism in Ref. [24].

The chiral magnetic effect arises in general in the presence of background magnetic fields B and a chiral imbalance, parameterized by a chiral chemical potential μ_5 . Besides the inhomogeneity of the magnetic field, it is realistic from a phenomenological point of view to consider the chiral imbalance to be non-uniform as well. In this letter, we will consider two scenarios including inhomogeneous magnetic fields: one with a uniform chiral chemical potential and one with μ_5 exhibiting a similar inhomogeneity as the magnetic field itself.

This letter is organized as follows: In Sec. II we discuss the relevant observables that we compute to study the CME as well as the details of the non-uniform magnetic background. This is followed by Sec. III, where we give the details of our simulation setup. Our results in full QCD are presented in Sec. IV for the homogeneous chiral imbalance, while in Sec. V, we briefly explore the scenario with inhomogeneous μ_5 . Finally, we conclude in Sec. VI. In a series of appendices, we provide an analytical calculation of our observable for free fermions, discuss the results with free staggered fermions, and give the details of our lattice implementations.

II. CME AND NON-UNIFORM MAGNETIC FIELDS

Throughout this letter, we consider QCD in thermal equilibrium, in the presence of a non-uniform background magnetic field pointing in the third spatial direction. In particular, we choose an x_1 -dependent profile of the form

$$\vec{B}(x_1) = B \cosh^{-2}(x_1/\epsilon) \vec{e}_3, \quad (1)$$

motivated by its analytical properties [25]. The parameter ϵ sets the width of the field profile and is chosen as ~ 0.6 fm in our QCD simulations, in order to make contact with the HIC situation [14]. Notice that the limit

$\epsilon \rightarrow \infty$ corresponds to the homogeneous profile. The profile (1) has already been used in QCD models [26], as well as on the lattice to study thermodynamics [15, 22].

The continuum electromagnetic current is defined as

$$j_\nu(x) = \sum_f \frac{q_f}{e} \bar{\psi}_f(x) \gamma_\nu \psi_f(x), \quad (2)$$

where $f = u, d, s, \dots$ labels the quark flavors, q_f are the corresponding electric charges and e is the elementary electric charge. Similarly, we consider the axial current

$$j_{\nu 5}(x) = \sum_f \bar{\psi}_f(x) \gamma_\nu \gamma_5 \psi_f(x), \quad (3)$$

associated with the total quark number, i.e. each quark flavor contributes with unit weight in it. The chiral chemical potential μ_5 , which parameterizes the chiral density, couples to the fourth component of Eq. (3). Below, we will also consider the currents averaged over a space-time slice, i.e. $J_\nu(x_1) \equiv T/L^2 \int d^4x' j_\nu(x') \delta(x_1 - x'_1)$ and similarly for $J_{\nu 5}(x_1)$.

To study the chiral magnetic effect on the lattice, we follow a similar approach as in our previous work [13], except that the magnetic field is not assumed to be homogeneous but is given by Eq. (1). To make contact with the heavy-ion-collision-inspired setups described in Sec. I, we define the most general form of the CME current in the presence of magnetic fields and chiral chemical potentials, where both depend on the x_1 coordinate. To linear order in μ_5 and in B , the current parallel to the magnetic field reads,

$$\langle J_3(x_1) \rangle = \int dx'_1 dx''_1 \chi_{\text{CME}}(x_1 - x'_1; x_1 - x''_1) eB(x'_1) \mu_5(x''_1), \quad (4)$$

involving the form factor χ_{CME} . In our simulations, which are performed at $\mu_5 = 0$ [27], it can be accessed via the first derivative,

$$\begin{aligned} H(x_1, x''_1) &\equiv \left. \frac{\delta \langle J_3(x_1) \rangle}{\delta \mu_5(x''_1)} \right|_{\mu_5=0} \\ &= \int dx'_1 \chi_{\text{CME}}(x_1 - x'_1; x_1 - x''_1) eB(x'_1), \end{aligned} \quad (5)$$

which describes the electromagnetic current generated at x_1 due to a weak chiral imbalance present at x''_1 . Note that $H(x_1, x''_1)$ depends on both arguments separately due to the breaking of translational invariance by the inhomogeneous magnetic field.

The response to a homogeneous chiral imbalance follows from replacing $\mu_5(x''_1)$ by μ_5 in Eq. (4), resulting in the integral of χ_{CME} over its second variable,

$$C_{\text{CME}}(x_1) = \int dx''_1 \chi_{\text{CME}}(x_1; x''_1), \quad (6)$$

which we refer to as the CME coefficient. For the homogeneous μ_5 setup, Eq. (5) simplifies to

$$G(x_1) \equiv \left. \frac{\partial \langle J_3(x_1) \rangle}{\partial \mu_5} \right|_{\mu_5=0} = \int dx'_1 C_{\text{CME}}(x_1 - x'_1) eB(x'_1), \quad (7)$$

which can also be constructed directly from Eq. (5) as $G(x_1) = \int dx''_1 H(x_1, x''_1)$. Equivalently, Eq. (7) in Fourier space reads

$$\tilde{G}(q_1) = \tilde{C}_{\text{CME}}(q_1) e\tilde{B}(q_1). \quad (8)$$

In the case of a homogeneous magnetic field, Eq. (7) trivially reduces to the global effect, parameterized by a single coefficient C_{CME} , which coincides with the zero momentum limit of Eq. (8), $\tilde{C}_{\text{CME}}(q_1 = 0)$. In Ref. [13], we showed that $C_{\text{CME}} = 0$ in full QCD, in accordance with the discussion in Sec. I and, in particular, with Bloch's theorem. As we will show below, this picture is not changed by an inhomogeneous field. However, while Bloch's theorem forbids global currents to flow in equilibrium, it allows the appearance of local currents, and hence non-vanishing G and H . Such local, x_1 -dependent currents are in the focus of our attention here. Our main discussion in Sec. IV revolves around G , while the more general behavior of H is discussed in Sec. V.

We note that for simplicity, we normalize our QCD results below by the overall proportionality factor $C_{\text{dof}} = N_c \sum_f (q_f/e)^2$, where $N_c = 3$ is the number of colors. In App. B, where we consider one colorless fermion flavor with charge e , this factor trivially reduces to 1.

III. LATTICE SETUP

In our lattice QCD simulations, we consider $2 + 1$ flavors of stout-smear rooted staggered fermions with physical masses. In this formalism, the partition function \mathcal{Z} can be written using the Euclidean path integral over the gluon links U ,

$$\mathcal{Z} = \int \mathcal{D}U \exp[-\beta S_g] \prod_f [\det M_f(U, q_f, m_f)]^{1/4}, \quad (9)$$

where the fermionic fields have already been integrated out to yield the fermion determinant, $\beta = 6/g^2$ denotes the inverse gauge coupling and m_f are the quark masses for each flavor $f = u, d, s$. In Eq. (9), S_g is the gluonic action, for which we use a tree-level improved Symanzik action, and M_f is the massive staggered Dirac operator, which contains the twice-stout-smear links and the quark charges $q_u/2 = -q_d = -q_s = e/3$. The quark masses are tuned to the physical point as a function of the lattice spacing a [28].

The simulations are performed on a four-dimensional lattice with N_s spatial and N_t temporal points. The physical spatial volume is given by $V = L^3 = (aN_s)^3$ and the temperature by $T = (aN_t)^{-1}$. At a fixed temperature, the continuum limit corresponds to $N_t \rightarrow \infty$. Note that the periodic spatial boundary conditions imply that the flux of the magnetic field is quantized. For our specific profile (1), this quantization condition takes the form [15],

$$eB = \frac{3\pi N_b}{\epsilon L \tanh(L/2\epsilon)}, \quad \text{where } N_b \in \mathbb{Z}. \quad (10)$$

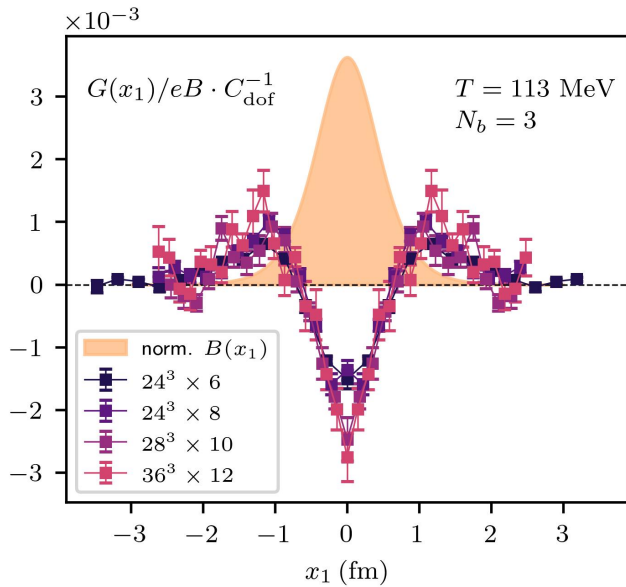


FIG. 1. Lattice data for the CME correlator in QCD as a function of x_1 at $T = 113$ MeV and $N_b = 3$ for different lattice spacings. The connecting lines serve to guide the eye. For comparison, the shaded area depicts the magnetic field profile from Eq. (1) in an arbitrary normalization.

Furthermore, we note that our setup does not include dynamical photons, i.e. the magnetic field is treated as a classical background field.

The derivative (7) – and the functional derivative (5) – of the current with respect to μ_5 results in a current-axial current correlator. We use the conserved (one-link) vector current and the anomalous axial (three-link) current in the staggered formulation [29]. We stress that for staggered quarks, care has to be taken when evaluating the μ_5 derivative of the current, for a tadpole term also appears. The exact form of the observables is given in App. C and a detailed discussion on the currents can be found in [13].

IV. HOMOGENEOUS CHIRAL CHEMICAL POTENTIAL

In this section, we discuss the results for the x_1 -dependence of the CME correlator (7) for a homogeneous μ_5 . For non-interacting fermions, $G(x_1)$ can be calculated analytically, see App. A. As a cross-check of our lattice setup, we computed the correlator for free staggered fermions as well. The continuum-extrapolated lattice results were found to match the analytic formula perfectly, serving as a validation of our lattice setup. The details of the lattice calculation for free staggered fermions are discussed in App. B.

After this cross-check, we continue by turning on color interactions and analyzing the results in full QCD. We

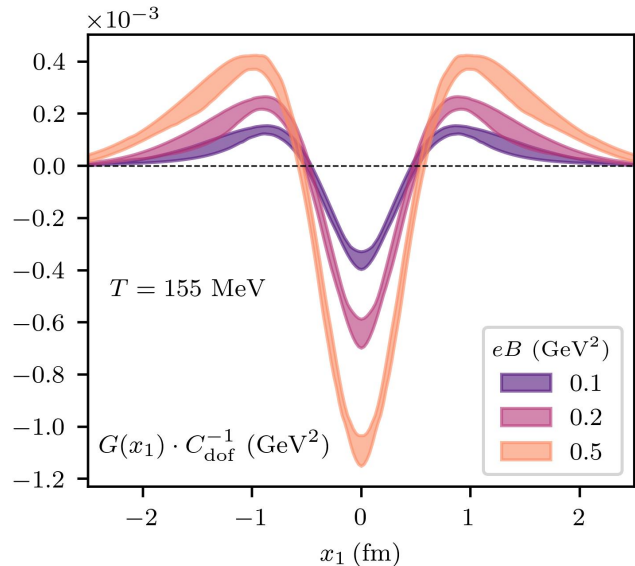


FIG. 2. Continuum limit of the CME correlator in QCD as a function of x_1 at $T = 155$ MeV. The bands show this correlator at three different magnetic field strengths: $eB = 0.1, 0.2$ and 0.5 GeV^2 .

take into account both connected and disconnected contributions to the CME correlator, see App. C. In Fig. 1, we show $G(x_1)$ as a function of x_1 for different lattice spacings and a weak magnetic field with profile width $\epsilon \approx 0.6$ fm. The figure shows that in this background, the CME correlator develops a non-trivial spatial structure, with the current flowing in opposite directions in the center ($x_1 \approx 0$) and towards the edges ($|x_1| \gtrsim \epsilon$). This behavior is similar to what we observed in the free case (see App. B). The current profile integrates to zero, implying that the global CME conductivity vanishes in equilibrium QCD, in agreement with our earlier findings [13].

Based on the results obtained on four different lattice spacings and different weak magnetic fields, we carry out the continuum extrapolation of $G(x_1)$, employing a multi-dimensional spline fit in x_1 , a and eB with node-points generated via Monte Carlo [30–32]. In Fig. 2, we show the so obtained continuum limit of the x_1 -dependent CME correlator for various values of eB . Finally, in Fig. 3, we show the CME correlator at the center ($x_1 = 0$) and near the edge ($x_1 = 0.9$ fm) as a function of the magnetic field. As one can see, the magnetic field dependence is practically unaffected by the temperature. It is tempting to quantify the inhomogeneous equilibrium effect by comparing to the expected out-of-equilibrium conductivity coefficient $1/(2\pi^2)$ [2]. In a small cell around the magnetic field peak, the current strength is given by the slope of the $x_1 = 0$ curve in Fig. 3, which for our setting we find to be $-1/(2\pi^2) \times 0.08(1)$. We stress that the so defined slope depends implicitly on the magnetic field profile.

Another interesting aspect of $G(x_1)$ is that sea effects,

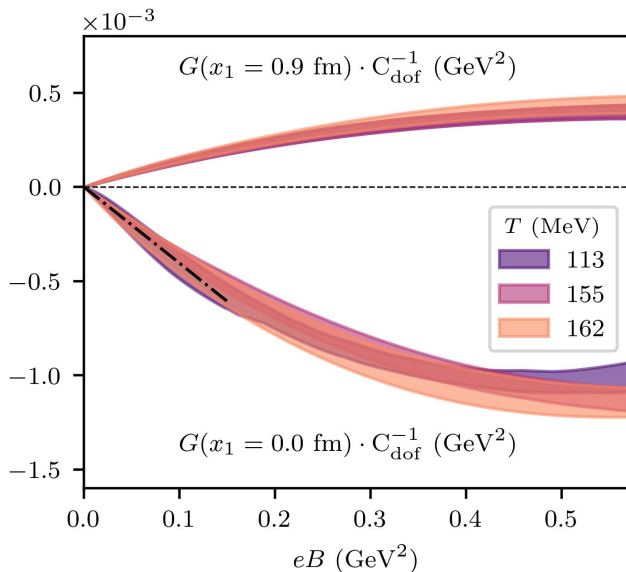


FIG. 3. CME correlator in the continuum limit at $x_1 = 0$ fm and at $x_1 = 0.9$ fm as a function of eB for temperatures below, at, and above the crossover. The weak-field behavior of the correlator at the center is indicated by the dot-dashed line.

i.e. magnetic field effects due to virtual quark loops, are found to be negligible, see App. C. This is analogous to what was found in the case of electric currents induced by inhomogeneous magnetic fields according to Ampère’s law in QCD [22]. Negligible sea effects imply that the CME correlator could also be computed on the lattice using a computationally cheaper technique, the so-called valence approximation, which we discuss in more detail in App. C.

V. BEYOND HOMOGENEOUS CHIRAL CHEMICAL POTENTIALS

Next, we consider the situation with an inhomogeneous chiral chemical potential $\mu_5(x'_1)$. The induced current at point x_1 is now given by the correlator $H(x_1, x'_1)$ from Eq. (5). This generalized correlator allows us to get a clearer picture of the role of μ_5 in the thermodynamic system. In particular, if a parametrization of the chiral imbalance profile is available, it permits a convolution between this profile and the two-point function, yielding a more realistic one-dimensional picture on how the CME current might behave in experiments.

In Fig. 4, we show the result for $H(x_1, x'_1)$ for a system of free fermions and for full QCD. In the latter case, we neglected the disconnected contributions, which were merely found to enhance the noise, see App. C. The plots reveal more details about the local CME currents generated at different coordinates and the cancellations taking place in the global current. The latter can be under-

stood by integrating over one of the two coordinates of $H(x_1, x'_1)$.

On the one hand, the sum over x'_1 corresponds to integrating out the spatial dependence of J_{45} , coming from μ_5 . As shown in the projection on the top axis of Fig. 4, this leads to a homogeneous μ_5 effect and agrees with the profiles that we computed before, see Fig. 1. On the other hand, summing over the x_1 coordinate corresponds to the zero-momentum component of J_3 (projection on the right axis in Fig. 4), which vanishes due to Bloch’s theorem [33].

VI. CONCLUSIONS

In this letter, we studied the local spatial structure of the chiral magnetic effect in equilibrium QCD with non-uniform magnetic background fields using first-principles lattice simulations. We found that in this setup – in contrast to the situation with homogeneous magnetic fields – nonzero electromagnetic currents flow in equilibrium. These CME currents are such that their spatial average vanishes, giving zero global current. Therefore, our results corroborate our earlier findings [13] that the global CME vanishes in equilibrium, and demonstrate a novel behavior of the chiral magnetic currents in the presence of non-uniform magnetic fields. From the theoretical point of view, it is intriguing to observe that the CME signal is realized as soon as the generalized Bloch theorem is circumvented by considering local currents instead of global ones. Regarding experiments, such inhomogeneous magnetic fields and local currents are certainly more realistic for off-central heavy-ion collisions.

Specifically, we analyzed the CME correlator, i.e. the current produced at x due to a chiral imbalance at x' and the inhomogeneous magnetic field. This correlator can be convoluted with a given ansatz for the chiral chemical potential profile to predict the spatial dependence of the induced current. Moreover, using the axial susceptibility χ_5 , the relationship between the chiral imbalance n_5 and the chiral chemical potential can also be constructed as $n_5 = \chi_5 \mu_5$. Using our results for χ_5 determined in [13], this allows one to predict CME signatures for a given fluctuation of chirality, leading to a more realistic description of the chiral magnetic current, sought after in experiments. This, alongside our one-dimensional profiles, may be used to guide future phenomenological studies of the CME in the presence of non-uniform magnetic fields.

Due to the highly inhomogeneous fields in HIC, our findings suggest that a signature of the CME might be revealed in off-central heavy-ion collision experiments specifically at mid-rapidities, where local magnetic fields are the strongest. Such signals could display the existence of topologically non-trivial fluctuations in the QCD matter produced in relativistic collisions.

Finally, we stress that in this work we focused exclusively on the static CME, present in QCD in equilibrium.

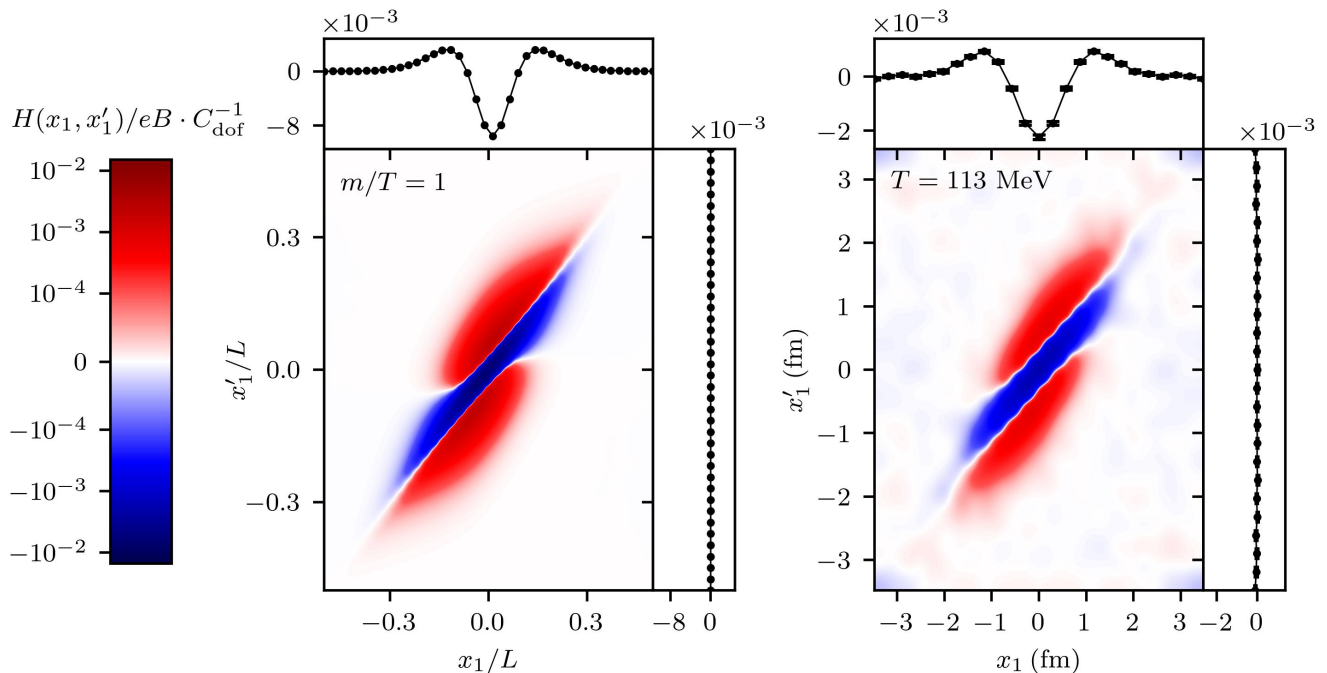


FIG. 4. Left panel: heat plot of the correlator $H(x_1, x'_1)$ normalized by eB in the free case in the $x_1 - x'_1$ plane for $m/T = 1$ on a $40^3 \times 10$ lattice. The color scheme is shown on a logarithmic scale for the absolute value of the observable from 0.015 to 10^{-4} , and a linear scale from the latter to 0. Red (blue) colors indicate the sign of the correlator. The projections on the top and right axes correspond to integrating over x'_1 and x_1 , respectively. Right panel: the connected part of the same observable in QCD at $T = 113 \text{ MeV}$ on a $24^3 \times 6$ lattice. To highlight the main features of the heat plot, the data was smoothed via a bicubic interpolation.

In contrast, time-dependent responses, generated by a time-dependent chiral imbalance, give rise to the out-of-equilibrium CME, which is more challenging to study using Euclidean lattice simulations, as these necessitate analytic continuation of Euclidean correlators [11].

Acknowledgements. This work was funded by the DFG (Collaborative Research Center CRC-TR 211 “Strong-interaction matter under extreme conditions” - project number 315477589 - TRR 211) and by the Helmholtz Graduate School for Hadron and Ion Research (HGS-HIRe for FAIR), as well as by STRONG-2020 “The strong interaction at the frontier of knowledge: fundamental research and applications” which received funding from the European Union’s Horizon 2020 research and innovation programme under grant agreement No 824093. The authors are grateful for enlightening discussions with Miklós Horváth, Xu-Guang Huang and Matthias Kaminski.

Appendix A: Free fermions with Pauli-Villars regularization

In this appendix, we calculate the CME coefficient required to construct the current signal in an inhomogeneous background magnetic field for a single, colorless fermion flavor with mass m and charge e . We carry out the calculation in Fourier space and obtain $\tilde{C}_{\text{CME}}(q_1)$ as used in Eq. (8). In principle, the calculation outlined could also be used for the more general case, where the chiral chemical potential is also space dependent, but here we only concentrate on the momentum dependence corresponding to the inhomogeneity of the magnetic field.

We start by writing down the axial vector-vector three-point correlator depending on two external momenta,

$$\langle j_{\mu 5}(-p - q) j_{\nu}(q) j_{\rho}(p) \rangle \equiv \Gamma_{\mu\nu\rho}^{\text{AVV}}(p + q, q, p) = -i \sum_{s=0}^3 c_s \int_K \frac{\text{Tr} [\gamma_{\mu} \gamma_5 (\not{K} + m_s) \gamma_{\nu} (\not{K} + \not{q} + m_s) \gamma_{\rho} (\not{K} + \not{q} + \not{p} + m_s)]}{(K^2 - m_s^2)((K + q)^2 - m_s^2)((K + q + p)^2 - m_s^2)} + (\{\nu, q\} \leftrightarrow \{\rho, p\}), \quad (\text{A1})$$

where we use Pauli-Villars regularization for QED following the textbook [34], see also [12]. This involves the physical fermion $s = 0$ with $c_0 = 1$ and $m_0^2 = m^2$, as well as the regulator fields $s > 0$ with $c_{1,2} = -c_3 = -1$, $m_{1,2}^2 = m^2 + \Lambda^2$ and $m_3^2 = m^2 + 2\Lambda^2$. The continuum limit entails taking $\Lambda \rightarrow \infty$. We also used the notation \int_K for a Matsubara summation and spatial integration over the loop momentum $K = (i\omega_n, \vec{k})$, with ω_n being the fermionic Matsubara frequencies at temperature T .

The three-point correlator $\Gamma_{\mu\nu\rho}^{\text{AVV}}(p+q, q, p)$ is the one appearing in the $U_A(1)$ anomaly: the famous formula can be recovered by contracting $\Gamma_{\mu\nu\rho}^{\text{AVV}}$ with $p^\mu + q^\mu$. Here, however, a different combination is relevant: we need to set the external momentum of the axial leg to zero

to ensure the homogeneity of μ_5 . In order to represent the equilibrium solution, we need to consider nonzero spatial momentum \vec{q} with $q_0 = 0$. To further simplify the calculation, we restrict ourselves to the case where the current and the magnetic field point in the x_3 direction. We choose a gauge for the magnetic field where only $A_2 \neq 0$. Hence, for the x_1 dependence we want to model, only a non-vanishing q_1 is needed. All in all, for the momentum dependent coefficient appearing in Eq. (8) we need to evaluate

$$\tilde{C}_{\text{CME}}(q_1) = \frac{1}{q_1} \Gamma_{023}^{\text{AVV}}(0, q_1, -q_1). \quad (\text{A2})$$

Evaluating the trace and taking the proper limits in Eq. (A1) yields

$$\tilde{C}_{\text{CME}}(q_1) = \frac{8}{q_1} \sum_{s=0}^3 c_s T \sum_n \int \frac{d^3k}{(2\pi)^3} \left[\frac{2q_1 m_s^2 - 2k_0^2 q_1}{(K^2 - m_s^2)^2 ((K+q)^2 - m_s^2)} + \frac{k_1 + q_1}{(K^2 - m_s^2)((K+q)^2 - m_s^2)} \right]_{k_0=i\omega_n}. \quad (\text{A3})$$

The summation over Matsubara frequencies leads to the Fermi-Dirac distribution $n_F(x) = (\exp(x/T) + 1)^{-1}$ and its derivative. After performing the angular integrals, we find

$$\tilde{C}_{\text{CME}}(q_1) = -\frac{1}{2\pi^2 q_1} \sum_{s=0}^3 c_s \int_0^\infty dk k \left(\frac{m_s^2(1/2 - n_F(E_{k,s}))}{E_{k,s}^3} - \frac{k^2}{E_{k,s}^2} n'_F(E_{k,s}) \right) \log \frac{(2k - q_1)^2}{(2k + q_1)^2}, \quad (\text{A4})$$

where we introduced $E_{k,s} = \sqrt{k^2 + m_s^2}$. The remaining integral over k can be carried out for the PV regulator fields, that is $s > 0$. The infinitely heavy fermions do not contribute to the T dependence, while in the vacuum their contribution is equivalent to taking $q_1 \rightarrow 0$, since the integral only depends on q_1/m_s . This zero-momentum limit for the regulator fields produces $-1/(2\pi^2)$. Our final formula for the momentum-dependent coefficient reads

$$\tilde{C}_{\text{CME}}(q_1) = -\frac{1}{2\pi^2} - \frac{1}{2\pi^2 q_1} \int_0^\infty dk k \left(\frac{m^2(1/2 - n_F(E_k))}{E_k^3} - \frac{k^2}{E_k^2} n'_F(E_k) \right) \log \frac{(2k - q_1)^2}{(2k + q_1)^2}, \quad (\text{A5})$$

with the physical energy $E_k = E_{k,0}$, which agrees with the results of [8] obtained in a slightly different way. The final integral has to be performed numerically. We note that the homogeneous magnetic field limit, that is $q_1 \rightarrow 0$, results in a vanishing coefficient through a double cancellation: the nonzero temperature part is zero separately for the physical fermion, while the vacuum term cancels due to the contribution of the PV fields. This confirms our previous findings regarding the vanishing of the CME current in equilibrium with homogeneous magnetic fields [13].

The inverse Fourier transform of Eq. (8), using $\tilde{C}_{\text{CME}}(q_1)$ from (A5) and the specific magnetic profile from Eq. (1) yields the CME correlator $G(x_1)$. This is shown by the black dashed line in Fig. 5 below.

One interesting observation is that the PV fields contribute only a constant shift to $\tilde{C}_{\text{CME}}(q_1)$. In other words, their contribution is a Dirac δ in coordinate space. This explains the shape of $G(x_1)$ in Fig. 5, where one

can recognize the sum of a sharp negative peak and a broader positive one. The former is the contribution of the regulator fields, for which the contact nature of $C_{\text{CME}}(x_1) \propto \delta(x_1)$ results in a current profile (4) directly proportional to $eB(x_1)$. In turn, for the physical fermion, the non-trivial q_1 dependence results in a smeared reaction to the magnetic profile in coordinate space.

Appendix B: Free fermions on the lattice

In this appendix we turn to the lattice discretization of Eq. (7) for non-interacting fermions. We again consider one colorless quark flavor with charge e and mass m . We will cross-check our lattice approach against the Pauli-Villars regularization discussed in App. A. The results for free fermions also reveal information about the high temperature limit of QCD, where it can be described in terms of a gas of free massless fermions.

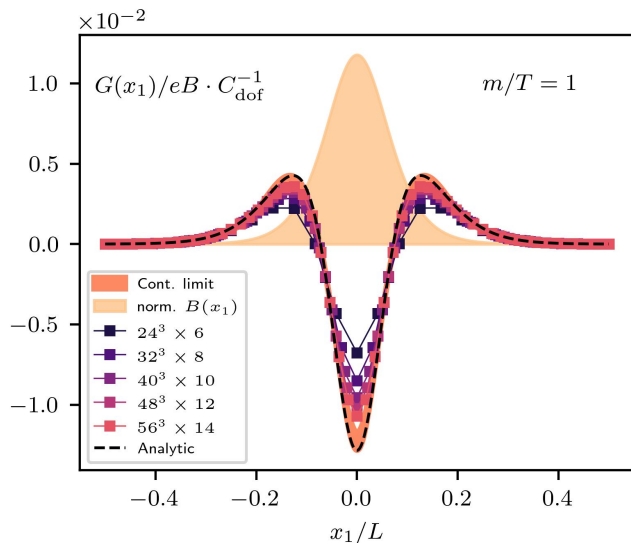


FIG. 5. Lattice data and continuum extrapolation of the CME correlator with $eB/T^2 = 14.14$ and $\epsilon T = 1/3$, normalized by the magnetic field, for free fermions. The analytical result is recovered in the continuum limit, confirming the validity of our setup. For comparison, the shaded area depicts the magnetic field profile (1) in arbitrary normalization.

For the lattice calculation, we use the exact eigensystem of the staggered Dirac operator, reconstructing the required matrix elements to calculate Eq. (7). This approach has the advantage of not relying on stochastic estimators for the traces, yielding an exact result for the x_1 dependence of the operator. For more details on the exact diagonalization, see Ref. [13].

Fig. 5 shows an example of the continuum extrapolation of the CME correlator for $m/T = 1$, $N_b = 2$ and aspect ratio $LT = 4$. The latter choice was found to be sufficiently close to the thermodynamic limit so that finite volume effects are negligible. The continuum limit agrees with the analytical calculation, validating our lattice implementation. The x_1 -integral of $G(x_1)$ is found to vanish – in other words, $\tilde{G}(q_1 = 0) = 0$, confirming that no global CME current flows in equilibrium.

Next, we discuss how the CME correlator is affected by the details of the magnetic profile. In Fig. 6, we show the impact of changing the magnitude (top panel) and the profile width (bottom panel) of the magnetic field. The middle point ($x_1 = 0$) scales linearly for weak B , a behavior that is found to persist in QCD as well (see Fig. 3 in the main text). Increasing ϵ , the shape of the CME correlator flattens, until a homogeneous B field is reached for $\epsilon \rightarrow \infty$. In this limit, we see that the correlator vanishes identically for every x_1 , confirming our earlier findings [13].

The vanishing of the global CME can be also understood in momentum space. In Fig. 7, we show the Fourier transform of the CME coefficient, as defined in Eq. (8). In this plot, the role of the regulator is most transparent.

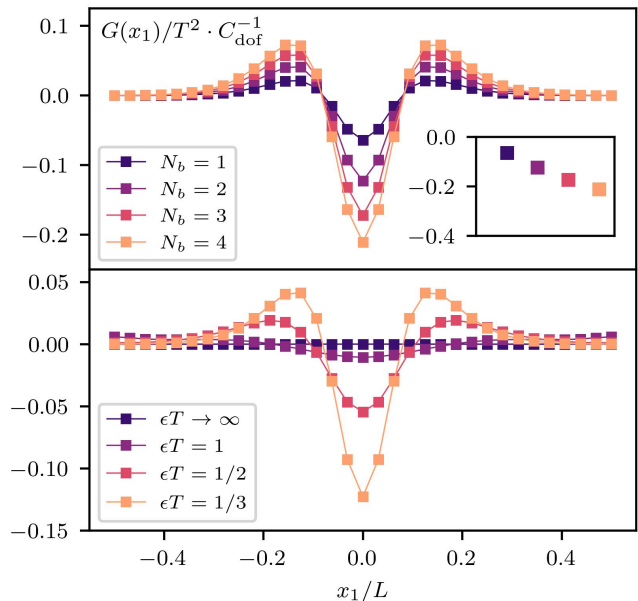


FIG. 6. Top panel: CME correlator for free fermions as a function of x_1/L for different values of N_b . The results correspond to a $32^3 \times 8$ lattice with $m/T = 1$ and $\epsilon T = 1/3$. The inset shows the magnetic field dependence of the central point. Bottom plot: ϵ dependence of the CME correlator, calculated on a $32^3 \times 8$ lattice with $m/T = 1$ and $N_b = 2$. Notice that the current vanishes in the limit of homogeneous magnetic fields, i.e. $\epsilon \rightarrow \infty$.

As we have seen in App. A, the Pauli-Villars regulator fields contribute $-1/(2\pi^2)$, and this value is approached in the infinite momentum limit. Together with this contribution, the total CME coefficient vanishes at zero momentum. Notice that the higher momentum components are increasingly more difficult to extract on the lattice, since large momenta cannot be resolved at finite lattice spacing. To determine the continuum limit, we fitted the data by including lattice artifacts up to quartic order in the lattice spacing and excluding the coarsest lattice. The systematic error was estimated by performing similar fits, considering $\mathcal{O}(a^2)$ lattice artifacts and including all data points. The so defined error is shown by the yellow band in Fig. 7. It is found to overlap with the analytical result, demonstrating again that finite volume effects in the lattice results are small.

Appendix C: Lattice implementations and valence approximation

In this appendix, we examine the valence and sea contributions to the impact of the magnetic field in the CME and introduce the valence approximation. Moreover, we specify the details of our implementation of the CME correlators introduced in the main text.

In the expectation value of any fermionic operator A

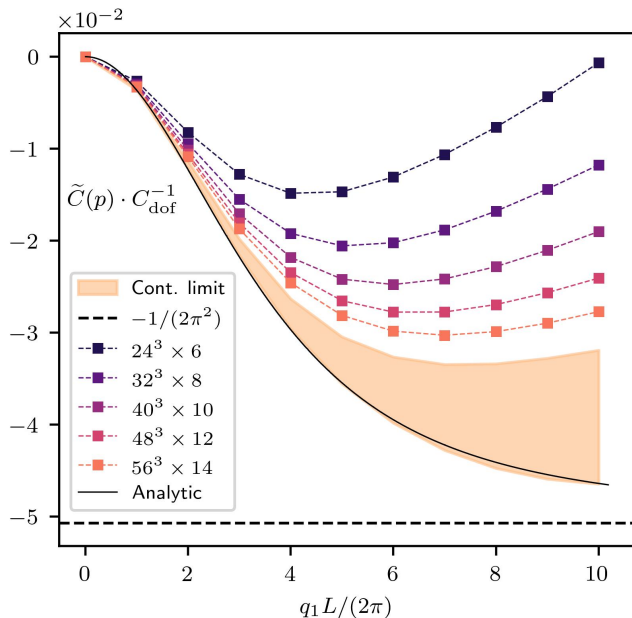


FIG. 7. Fourier transform of the CME coefficient as a function of the momentum for different lattice sizes. The solid line represents the analytical result. In the infinite-momentum limit, the result converges to $-1/(2\pi^2)$, which arises purely from the Pauli-Villars regulator fields in the analytic calculation.

with respect to (9), the dependence on the magnetic field enters in two distinct ways: in the operator (valence contribution) and in the fermion determinant (sea contribution),

$$\langle A \rangle = \int \mathcal{D}U \frac{e^{-\beta S_g}}{\mathcal{Z}(B)} \prod_f [\det M_f(B)]^{1/4} A(B). \quad (\text{C1})$$

The B dependence in the operator appears via quark propagators $M_f^{-1}(B)$. Thus, in a perturbative language, the valence effect arises due to the coupling of the magnetic field to the valence quark propagator, while the sea effect is due to the coupling to virtual quark loops. More

specifically, the valence contribution reads

$$\langle A \rangle^{\text{val}} = \int \mathcal{D}U \frac{e^{-\beta S_g}}{\mathcal{Z}(B=0)} \prod_f [\det M_f(B=0)]^{1/4} A(B). \quad (\text{C2})$$

Conversely, the sea contribution corresponds to setting $B=0$ in the operator, but keeping it in the determinants,

$$\langle A \rangle^{\text{sea}} = \int \mathcal{D}U \frac{e^{-\beta S_g}}{\mathcal{Z}(B)} \prod_f [\det M_f(B)]^{1/4} A(B=0). \quad (\text{C3})$$

For weak magnetic fields, expectation values $\langle A \rangle$ can be approximately decomposed into their valence $\langle A \rangle^{\text{val}}$ and sea $\langle A \rangle^{\text{sea}}$ contributions. For expectation values that are odd in the magnetic field – like the CME current or the CME correlators – this weak-field leading-order additivity relation takes the form [22][35],

$$\langle A \rangle = \langle A \rangle^{\text{val}} + \langle A \rangle^{\text{sea}} + \mathcal{O}(B^3). \quad (\text{C4})$$

Often one finds empirically that the valence contribution dominates this sum so that $\langle A \rangle \approx \langle A \rangle^{\text{val}}$ at leading order. This is the valence approximation, which we investigate below for the CME correlator as observable.

To do so, we give a detailed definition of our observables: the current and the CME correlators. In the staggered formalism, the electric current expectation value reads

$$\langle J_\nu(x_1) \rangle = \frac{T}{4L^2} \sum_f \frac{q_f}{e} \left\langle \text{Tr} \left(\mathcal{P}_{x_1} \Gamma_\nu^f M_f^{-1}(B) \right) \right\rangle, \quad (\text{C5})$$

where the trace entails sums over color and space-time coordinates and \mathcal{P}_{x_1} denotes a projector to the slice of the lattice, where the first spatial coordinate equals x_1 . In Eq. (C5), the staggered Dirac matrices Γ_ν^f appear. For their explicit form in the presence of B and μ_5 , see Ref. [13]. We will also need the staggered equivalents of the $\gamma_\nu \gamma_5$ matrices [29],

$$\Gamma_{\nu 5}^f \equiv \frac{1}{3!} \sum_{\rho\alpha\beta} \epsilon_{\nu\rho\alpha\beta} \Gamma_\rho^f \Gamma_\alpha^f \Gamma_\beta^f. \quad (\text{C6})$$

Its $\nu=4$ component couples to μ_5 in the Dirac operator in an exponential form [13].

To obtain the correlator (5), we need to perform the functional derivative of (C5) with respect to $\mu_5(x'_1)$. The chiral chemical potential appears in M_f^{-1} , in the determinants under the expectation value, in the normalization $\mathcal{Z}(B)$, as well as in Γ_ν^f [13]. Altogether, we arrive at

$$\begin{aligned}
H(x_1, x'_1) \equiv & \frac{T}{4L^2} \sum_f \left[\frac{1}{4} \sum_{f'} q_f q_{f'} \left\langle \text{Tr} \left[\mathcal{P}_{x_1} \Gamma_3^f M_f^{-1}(B) \right] \text{Tr} \left[\mathcal{P}_{x'_1} \Gamma_{45}^{f'} M_{f'}^{-1}(B) \right] \right\rangle_B \right. \\
& \left. - q_f^2 \left\langle \text{Tr} \left[\mathcal{P}_{x_1} \Gamma_3^f M_f^{-1}(B) \mathcal{P}_{x'_1} \Gamma_{45}^f M_f^{-1}(B) \right] \right\rangle_B + q_f^2 \left\langle \text{Tr} \left[\mathcal{P}_{x_1} \frac{\delta \Gamma_3^f}{\delta \mu_5(x'_1)} M_f^{-1}(B) \right] \right\rangle_B \right]. \quad (\text{C7})
\end{aligned}$$

Here we used that $\langle J_3(x_1) \rangle$ vanishes at $\mu_5 = 0$, leaving the three terms on the right hand side, which we refer to as disconnected, connected and tadpole terms, respectively. For clarity, in Eq. (C7) we indicated that the expectation values are to be evaluated at nonzero B . The so calculated observable is shown in Fig. 4 of the main text, except that in the QCD case we ignored the disconnected contribution to it, which was merely found to dominate the statistical errors (see below).

Summing over the x'_1 coordinate (i.e. the coordinate corresponding to the μ_5 insertion) in (C7) yields the correlator $G(x_1)$, in accordance with Eq. (7). The valence approximations, $H^{\text{val}}(x_1, x'_1)$ and $G^{\text{val}}(x_1)$ of these correlators are obtained with the same operators evaluated at $B = 0$, i.e. using the $B = 0$ ensemble of gauge configurations, just like in the general case (C2). Moreover, we also consider the correlator without the disconnected term (evaluated at $B > 0$), i.e. just the second and third terms in Eq. (C7), and $G^{\text{conn+tadp}}$ calculated from it.

In Fig. 8 we compare $G(x_1)$, $G^{\text{val}}(x_1)$ and $G^{\text{conn+tadp}}(x_1)$ in QCD for two different temperatures and magnetic fields. In both cases we observe a remarkable agreement among all three quantities, which we found to hold for all other simulation points as well. Interestingly, we observed the valence approximation to be valid even in the strong-field regime. In fact, we verified the approximate equality between the full and valence observables for magnetic fields as strong as $eB/T^2 \approx 83$ at $T = 113$ MeV, and $eB/T^2 \approx 114$ at $T = 155$ MeV.

Altogether, these findings demonstrate that the sea effect is strongly suppressed compared to the valence one in this observable and, moreover, the disconnected terms – contributing the most to the noise – are also negligible. Since the valence approximation significantly reduces the computational costs, this approximation is suitable for studies involving more expensive fermion actions, such as Wilson, domain-wall, and overlap fermions, in the presence of background magnetic fields.

-
- [1] D. E. Kharzeev, J. Liao, and P. Tribedy, Chiral Magnetic Effect in Heavy Ion Collisions: The Present and Future, (2024), [arXiv:2405.05427 \[nucl-th\]](#).
 - [2] K. Fukushima, D. E. Kharzeev, and H. J. Warringa, The Chiral Magnetic Effect, *Phys. Rev. D* **78**, 074033 (2008), [arXiv:0808.3382 \[hep-ph\]](#).
 - [3] Q. Li, D. E. Kharzeev, C. Zhang, Y. Huang, I. Pletikosic, A. V. Fedorov, R. D. Zhong, J. A. Schneeloch, G. D. Gu, and T. Valla, Observation of the chiral magnetic effect in ZrTe₅, *Nature Phys.* **12**, 550 (2016), [arXiv:1412.6543 \[cond-mat.str-el\]](#).
 - [4] L. Adamczyk *et al.* (STAR), Fluctuations of charge separation perpendicular to the event plane and local parity violation in $\sqrt{s_{NN}} = 200$ GeV Au+Au collisions at the BNL Relativistic Heavy Ion Collider, *Phys. Rev. C* **88**, 064911 (2013), [arXiv:1302.3802 \[nucl-ex\]](#).
 - [5] L. Adamczyk *et al.* (STAR), Beam-energy dependence of charge separation along the magnetic field in Au+Au collisions at RHIC, *Phys. Rev. Lett.* **113**, 052302 (2014), [arXiv:1404.1433 \[nucl-ex\]](#).
 - [6] M. Abdallah *et al.* (STAR), Search for the chiral magnetic effect with isobar collisions at $\sqrt{s_{NN}}=200$ GeV by the STAR Collaboration at the BNL Relativistic Heavy Ion Collider, *Phys. Rev. C* **105**, 014901 (2022), [arXiv:2109.00131 \[nucl-ex\]](#).
 - [7] N. Yamamoto, Generalized Bloch theorem and chiral transport phenomena, *Phys. Rev. D* **92**, 085011 (2015), [arXiv:1502.01547 \[cond-mat.mes-hall\]](#).
 - [8] D. Hou, H. Liu, and H.-c. Ren, Some Field Theoretic Issues Regarding the Chiral Magnetic Effect, *JHEP* **05**, 046, [arXiv:1103.2035 \[hep-ph\]](#).
 - [9] P. V. Buividovich, Anomalous transport with overlap fermions, *Nucl. Phys. A* **925**, 218 (2014), [arXiv:1312.1843 \[hep-lat\]](#).
 - [10] M. A. Zubkov, Absence of equilibrium chiral magnetic effect, *Phys. Rev. D* **93**, 105036 (2016), [arXiv:1605.08724 \[hep-ph\]](#).
 - [11] P. V. Buividovich, Out-of-equilibrium Chiral Magnetic Effect from simulations on Euclidean lattices, (2024), [arXiv:2404.14263 \[hep-lat\]](#).
 - [12] M. Horváth, D. Hou, J. Liao, and H.-c. Ren, Chiral magnetic response to arbitrary axial imbalance, *Phys. Rev. D* **101**, 076026 (2020), [arXiv:1911.00933 \[hep-ph\]](#).
 - [13] B. B. Brandt, G. Endrődi, E. Garnacho-Velasco, and G. Markó, On the absence of the chiral magnetic effect in equilibrium QCD, *JHEP* **09**, 092, [arXiv:2405.09484 \[hep-lat\]](#).
 - [14] W.-T. Deng and X.-G. Huang, Event-by-event generation of electromagnetic fields in heavy-ion collisions, *Phys. Rev. C* **85**, 044907 (2012), [arXiv:1201.5108 \[nucl-th\]](#).
 - [15] B. B. Brandt, F. Cuteri, G. Endrődi, G. Markó, L. Sandbote, and A. D. M. Valois, Thermal QCD in a non-uniform magnetic background, *JHEP* **11**, 229, [arXiv:2305.19029 \[hep-lat\]](#).

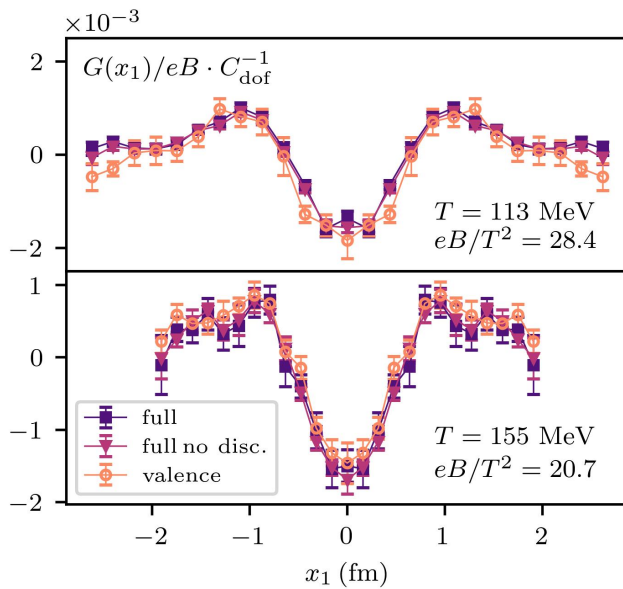


FIG. 8. Comparison between the full correlator $G(x_1)$, its valence contribution $G^{\text{val}}(x_1)$ and the full correlator without disconnected contributions, $G^{\text{conn+tdp}}(x_1)$, for a given magnetic field strength at low T (upper plot) and at the crossover temperature (lower plot). The correlators are normalized by the magnetic field.

[16] P. V. Buividovich, M. N. Chernodub, E. V. Luschevskaya, and M. I. Polikarpov, Numerical evidence of chiral magnetic effect in lattice gauge theory, *Phys. Rev. D* **80**, 054503 (2009), [arXiv:0907.0494 \[hep-lat\]](#).

[17] A. Yamamoto, Chiral magnetic effect in lattice QCD with a chiral chemical potential, *Phys. Rev. Lett.* **107**, 031601 (2011), [arXiv:1105.0385 \[hep-lat\]](#).

[18] A. Yamamoto, Lattice study of the chiral magnetic effect in a chirally imbalanced matter, *Phys. Rev. D* **84**, 114504 (2011), [arXiv:1111.4681 \[hep-lat\]](#).

[19] P. V. Buividovich, D. Smith, and L. von Smekal, Numerical study of the chiral separation effect in two-color QCD at finite density, *Phys. Rev. D* **104**, 014511 (2021), [arXiv:2012.05184 \[hep-lat\]](#).

[20] M. Pühr and P. V. Buividovich, The Chiral Separation Effect in quenched finite-density QCD, *EPJ Web Conf.* **175**, 04003 (2018), [arXiv:1712.01579 \[hep-lat\]](#).

[21] B. B. Brandt, G. Endrődi, E. Garnacho-Velasco, and G. Markó, The chiral separation effect from lattice QCD at the physical point, *JHEP* **02**, 142, [arXiv:2312.02945 \[hep-lat\]](#).

[22] B. B. Brandt, G. Endrődi, G. Markó, and A. D. M. Valois, Steady electric currents in magnetized QCD and

their use for the equation of state, *JHEP* **07**, 027, [arXiv:2405.06557 \[hep-lat\]](#).

[23] G. Endrődi, QCD with background electromagnetic fields on the lattice: a review, (2024), [arXiv:2406.19780 \[hep-lat\]](#).

[24] C. Banerjee, M. Lewkowicz, and M. A. Zubkov, Equilibrium chiral magnetic effect: Spatial inhomogeneity, finite temperature, interactions, *Phys. Lett. B* **819**, 136457 (2021), [arXiv:2105.11391 \[hep-ph\]](#).

[25] G. V. Dunne, Heisenberg-Euler effective Lagrangians: Basics and extensions, in *From fields to strings: Circumnavigating theoretical physics. Ian Kogan memorial collection (3 volume set)*, edited by M. Shifman, A. Vainshtein, and J. Wheeler (2004) pp. 445–522, [arXiv:hep-th/0406216](#).

[26] G. Cao, Chiral symmetry breaking in a semilocalized magnetic field, *Phys. Rev. D* **97**, 054021 (2018), [arXiv:1801.00134 \[nucl-th\]](#).

[27] Although simulations at non-zero chiral chemical potential are free of the sign problem on the lattice, there are technical difficulties that arise when implementing μ_5 in the staggered fermion formulation, which is the reason why we consider the first derive of the current with respect to μ_5 . See [13] for a detailed discussion.

[28] S. Borsányi, G. Endrődi, Z. Fodor, A. Jakovác, S. D. Katz, S. Krieg, C. Ratti, and K. K. Szabó, The QCD equation of state with dynamical quarks, *JHEP* **11**, 077, [arXiv:1007.2580 \[hep-lat\]](#).

[29] S. Dürr, Taste-split staggered actions: eigenvalues, chiralities and Symanzik improvement, *Phys. Rev. D* **87**, 114501 (2013), [arXiv:1302.0773 \[hep-lat\]](#).

[30] G. Endrődi, Multidimensional spline integration of scattered data, *Comput. Phys. Commun.* **182**, 1307 (2011), [arXiv:1010.2952 \[physics.comp-ph\]](#).

[31] B. B. Brandt, F. Cuteri, and G. Endrődi, Equation of state and speed of sound of isospin-asymmetric QCD on the lattice, *JHEP* **07**, 055, [arXiv:2212.14016 \[hep-lat\]](#).

[32] B. B. Brandt and G. Endrődi, QCD phase diagram with isospin chemical potential, *PoS LATTICE2016*, 039 (2016), [arXiv:1611.06758 \[hep-lat\]](#).

[33] We note that Bloch’s theorem [7] holds in the infinite volume limit. On a finite volume, we find that the sum of the profile in x_1 does give a nonzero signal, even though it is four orders of magnitude smaller than the one obtained by summing over x'_1 . This signal is similar to the one found for the quark condensate in [36], and vanishes in the thermodynamic limit.

[34] C. Itzykson and J. B. Zuber, *Quantum Field Theory*, International Series In Pure and Applied Physics (McGraw-Hill, New York, 1980).

[35] For expectation values even in B , a similar decomposition can also be derived [22].

[36] P. Adhikari and B. C. Tiburzi, QCD thermodynamics and neutral pion in a uniform magnetic field: Finite volume effects, *Phys. Rev. D* **107**, 094504 (2023), [arXiv:2302.09179 \[hep-lat\]](#).